LIP-STUDENTS-25-06

Characterisation of Sealed RPC Chambers

Catarina Tomé[1,a] , Joana Cruz[1,b] , Laura Carvalho[1,c] and Telmo Paes[1,d]

[1] *Departamento de Física, Universidade de Coimbra, Coimbra, Faculdade de Ciências e Tecnologia, Portugal*

Project supervisor: Alberto Blanco Castro

January 20, 2026

Abstract. The gases used in Resistive Plate Chambers (RPCs), which belong to the hydrofluorocarbon class, present an environmental challenge due to their significant contribution to the greenhouse effect. In response to increasingly stringent regulations, sRPCs (sealed RPCs) have emerged as an innovative technological solution, characterized by their operation without requiring gas supply or recirculation systems. In this work, we study the impact of variations in environmental parameters, such as pressure and temperature, on the detector response. This study is of particular importance since, a priori, a sealed detector is expected to behave differently from an atmospheric detector.

Keywords: sRPC, Muon detection, Environmental Effects

1 Introduction

Resistive Plate Chambers (RPCs) have become a cornerstone technology in high-energy physics experiments, valued for their exceptional timing resolution, large active areas, and cost-effectiveness. However, their conventional operation relies on gas mixtures containing hydrofluorocarbons (HFCs), which face increasing environmental restrictions due to their global warming potential.

The growing regulatory pressure has driven the development of sealed RPCs (sRPCs), which eliminate the need to operate the detector in flux mode while maintaining detector functionality. Operation in sealed mode must be well understood, as a priori a sealed detector is expected to respond differently from an atmospheric detector to environmental variations such as pressure and temperature.[1, 2]. These effects become particularly relevant for applications requiring stable operation in uncontrolled environments, such as cosmic ray [3] or portable detection systems as in Figure1.

This study presents a systematic investigation of environmental effects in a multi-gap sRPC prototype. Through controlled measurements and long-term monitoring, we characterize the detector's performance under varying conditions, providing crucial insights for the development of future sealed systems. Our findings establish a foundation for reliable sRPC operation in diverse experimental configurations where gas infrastructure is impractical.

2 Experimental Setup

The experimental setup for this study consists of a sealed Resistive Plate Chamber (sRPC) module, a muon telescope for triggering, and a dedicated data acquisition (DAQ) system, Figure 1. This section provides a detailed description of each component and their integration.

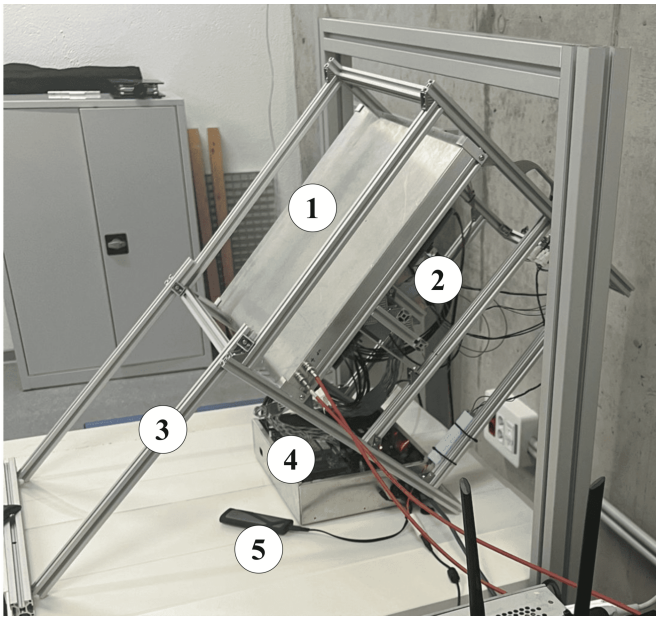

Figure 1: Assembly of setup detection with components: 1. sRPC; 2. SiPMs; 3. Aluminium Structure; 4. DAQ; 5. Extra Unity nVMe M.2 SSD.

2.1 Sealed Resistive Plate Chamber (sRPC) Module

The sealed Resistive Plate Chamber (sRPC) employed in this study consists of a multi-gap configuration specifically designed to operate without continuous gas circulation. The active structure incorporates two gas gaps, each 1 mm thick, defined by three 2 mm-thick soda-lime glass electrodes. Each electrode plate has a surface area of 350×350 mm^2. The soda-lime glass used for the electrodes exhibits a bulk resistivity of approximately 5×10^{12} Ωcm at 25°C. Mechanical stability and uniform gap spacing are achieved through the inclusion of a circular spacer, 10 mm in diameter, positioned at the center of the active area of each gap. In addition, a 25 mm wide strip spacer runs along the perimeter, ensuring rigidity and maintaining the separation between the electrodes.

Assembly of the detector is carried out under controlled pressure conditions. All peripheral interfaces are sealed with epoxy adhesive to guarantee both hermetic closure and structural robustness. Each gas gap is equipped with independent

[a] e-mail: catarinadiastome@gmail.com
[b] e-mail: joanacardosocruz@gmail.com
[c] e-mail: carvalho05laura@gmail.com
[d] e-mail: telmopbjunior@gmail.com

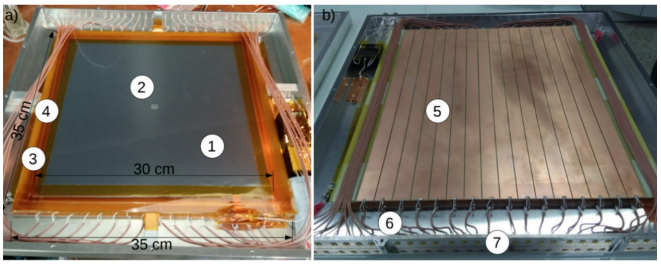

Figure 2: The interior of the sRPC. 1. HV layer, 2. Circular spacer in the center of the active area, 3. Strip spacer all around the periphery, 4. Mylar and Kapton layers, 5. Readout strip plane, 6. Coaxial cables and 7. MMCX RF feedthrough connectors.

gas inlet and outlet feedthroughs, initially used for flushing with the working mixture of 97.5% $C_2H_2F_4$ and 2.5% SF_6 at a controlled flow of 4 cm^3/min. After a few days of circulation, the feedthroughs are permanently sealed, leaving the chamber ready for operation in a closed-gas configuration. High voltage is applied to the outer glass plates via a semiconductive coating applied by airbrushing acrylic paint with a surface resistivity of approximately 100 MΩ/□. This layer covers a central region of 300×300 mm^2 and is subsequently insulated with protective layers of Mylar™ and Kapton™.

The readout system consists of sixteen copper strips arranged on a Flame Retardant 4 (FR4) printed circuit board located on the top surface of the chamber. The strips are 18 mm wide, spaced with a 19 mm pitch, and extend across the active area. Each strip is connected at both ends to the central conductor of a coaxial cable, with the shielding connected to a ground plane placed beneath the sRPC. Two of the strips are grounded and not read out (n order to leave channels available for the readout of the muon telescope). This configuration results in 14 active strips, corresponding to 28 signals routed to the front-end electronics.

The entire assembly, including the electrode stack and the readout structure, is enclosed in an aluminum housing. This enclosure provides mechanical protection and electromagnetic shielding. All coaxial cables are terminated with MMCX RF connectors to interface with the subsequent electronic processing stages.

2.2 Muon Telescope

Detection of atmospheric muons was performed using a compact plastic scintillator telescope. The telescope consists of four scintillator units, each with dimensions of $40 \times 40 \times 10$ mm^3. Each scintillator is coupled on one of its smaller faces to a Silicon Photomultiplier (SiPM) for light readout. The scintillators are arranged in a vertical stack, forming a geometry that defines a precise acceptance window for incident muons.

The sRPC module is positioned at an inclination of 45° relative to the horizontal plane, with the telescope placed directly behind it, see Figure1. To refine the geometrical acceptance, Styrofoam blocks are inserted between the scintillators. This mechanical configuration enhances directional selectivity by suppressing signals from particles arriving at oblique angles outside the region of interest. With this setup, the telescope serves as an independent external trigger, ensuring that all recorded coincidence events correspond to muons traversing the sRPC.

2.3 Electronics

The fFEE, originally developed for the HADES RPC-TOF detector, amplifies and shapes the incoming pulses. In this configuration, the SiPM was operated without an additional amplification stage since its output signal provides sufficient intrinsic amplitude for the data acquisition system. This approach contrasts with that required for RPC detectors, which demand amplification due to significantly lower signal levels. The insertion of an amplifier into the SiPM circuit would saturate the readout system, preventing the distinction between the charge levels of the pulses and, consequently, compromising the quantitative measurement of this parameter.

The outputs are provided in Low-Voltage Differential Signaling (LVDS) format, where the leading edge encodes the event time and the pulse width is proportional to the induced charge signal. Digital signals from the fFEE are transmitted to a TRB3SC1 board, which contains thirty-two multi-hit Time-to-Digital Converter (TDC) channels implemented in an FPGA. This TDC system offers a time precision better than 20 ps. The trigger logic implemented in the FPGA allows flexible operation, supporting both external triggering based on muon coincidences in the plastic scintillator telescope and internal self-triggering using only sRPC signals. The TRB3SC1 board [4], which handles the time digitization and trigger logic, is integrated into a compact aluminium enclosure alongside a single-board computer and auxiliary systems, see Figure3. These include low-voltage power supplies and environmental sensors for monitoring temperature, pressure, and relative humidity. This arrangement results in a fully autonomous and portable data acquisition unit, well-suited for deployment in both laboratory and field environments.

3 Experimental procedure

3.1 Signal Readout and Position Reconstruction

The sRPC strips are read out from both ends through the Front-End Electronics (FEE), providing independent "front" (F) and "back" (B) signals for each channel. From these signals, two key physical quantities are extracted: the signal time T and the signal charge Q. The time T is obtained from the leading edge of the LVDS output, with a precision better than 20 ps. The charge Q is determined from the pulse width using the Time over Threshold (ToT) method, applied to an integrated copy (with a 100 ns integration time) of the original signal.

For each strip that registers a signal, individual values of Q and T are obtained separately for the front and back readouts. The average of the front and back values, $(TF + TB)/2$ and $(QF + QB)/2$, represents the signal time and charge on that particular strip. The transverse position X of the particle is assigned to the location of the strip with the maximum charge, whereas the longitudinal coordinate Y along that strip is computed from the time difference between front and back readouts, $(TF - TB)$, multiplied the known signal propagation

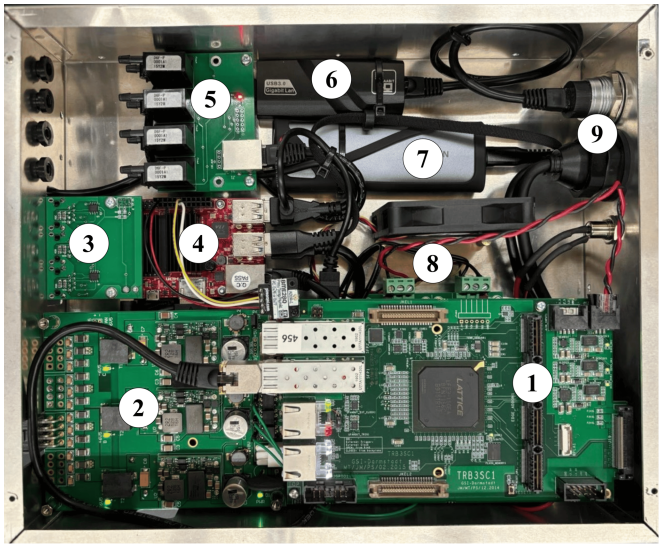

Figure 3: DAQ system and intern circuits: 1. FPGA Board TRB3SC1; 2. LV Power System of the fFEE; 3. I^2C distribuition board; 4. Mini-PC, 5. Gas Sensor Module (not ussed) , 6. USB to Ethernet Adapter; 7. NVMe M.2 SSD; 8. Relay Control Board; 9. Power and computer connections.

velocity of 165 mm/ns. To ensure accuracy, strip-specific time offsets measured during calibration are applied to the result. Additionally, charge and timing information is also recorded for the four scintillators used in the muon telescope. To determine how the total charge per event should be calculated, we first analysed the signal multiplicity across the readout strips.

3.2 Multiplicity Analysis

Multiplicity is defined as the number of strips that register a signal in a single event (considering front and back signals). The histogram in Figure 4 shows that most events produce signals in three or four strips. This is expected due to the natural spreading of induced charge over adjacent electrodes and capacitive coupling effects, which lead to signal sharing between neighbouring strips. Lower multiplicities (1–2 strips) are less common, while very high multiplicities are rare and typically associated with residual noise or spurious effects. Understanding multiplicity is crucial for accurate event reconstruction, particularly for a more precise determination of the total induced charge [3].

3.3 Total Charge Induce per Event

In earlier analyses, the event charge was typically defined using only the single strip with the highest recorded signal, a simplified approach adopted for practical reasons. However, in order to improve acuraciness we adapted this approach by summing the two highest charges per event.

To validate this approach, we investigated the charge distribution of individual strips within an event, ordered by their signal amplitude. Figure 5a presents the histograms of the 1^{st} and 2^{nd} largest charges recorded per event, which represent the dominant contributions to the total induced charge. In contrast, Figure 5b displays the histograms of the 3^{rd} and 4^{th}

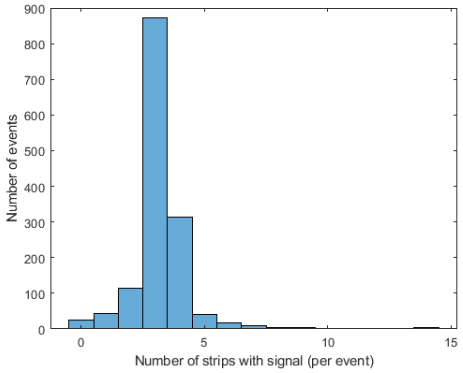

Figure 4: Multiplicity distribution of sRPC events, showing the number of strips registering a signal per event.

largest charges per event. All histograms are plotted with a common charge range of 0 to 150 pC for direct visual comparison.

As observed in Figure 5b, the contributions from additional strips (beyond the two strongest signals) are typically very small, concentrating at values close to zero. This suggests that these minor signals are predominantly due to crosstalk tails, which add little to the reconstructed charge and can increase measurement uncertainty.

Summing only the two dominant strips captures the majority of the induced charge.

3.4 Muon Event Selection

To isolate atmospheric muon events, a three-stage filtering process was applied to the coincidence signals from the muon telescope, aimed at suppressing contributions from random background, electronic noise, and non-muon radiation.

- **Coincidence requirement:** Events had to trigger all four scintillators simultaneously.
- **Timing consistency check:** The time difference between the top and bottom scintillators was analyzed. A Gaussian fit was used to estimate the expected distribution for relativistic muons. Events falling outside an acceptance window (mean $\pm$ 2 $\times$ FWHM) were excluded, effectively removing accidental coincidences and non-muon backgrounds.
- **Charge consistency filtering:** For each scintillator, a Gaussian fit to the charge distribution was performed. Only events with charges within the range (mean $\pm$ 2 $\times$ FWHM) were retained, removing noisy or saturated events and also removing muons that passed at the edge of the scintillators, which futher restricts the acceptance.

After these steps, the remaining dataset constitutes a clean sample of atmospheric muon candidates, serving as the reference trigger for evaluating sRPC performance.

3.5 Detector Efficiency and Performance Maps

For the efficiency and performance studies, the sRPC was operated at a voltage of 6 kV. This value corresponds to the

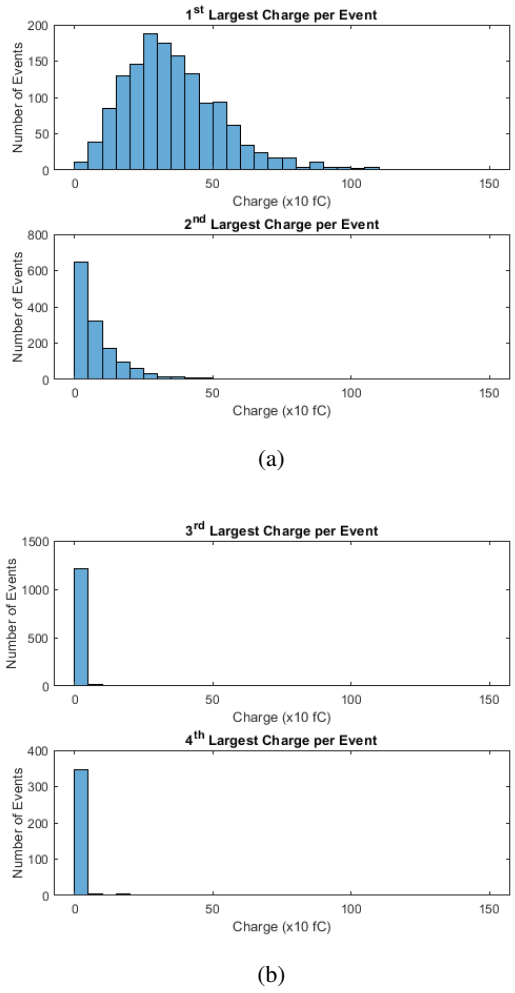

Figure 5: (a) Histograms of the 1st and 2nd largest charges per event. (b) Histograms of the 3rd and 4th largest charges per event.

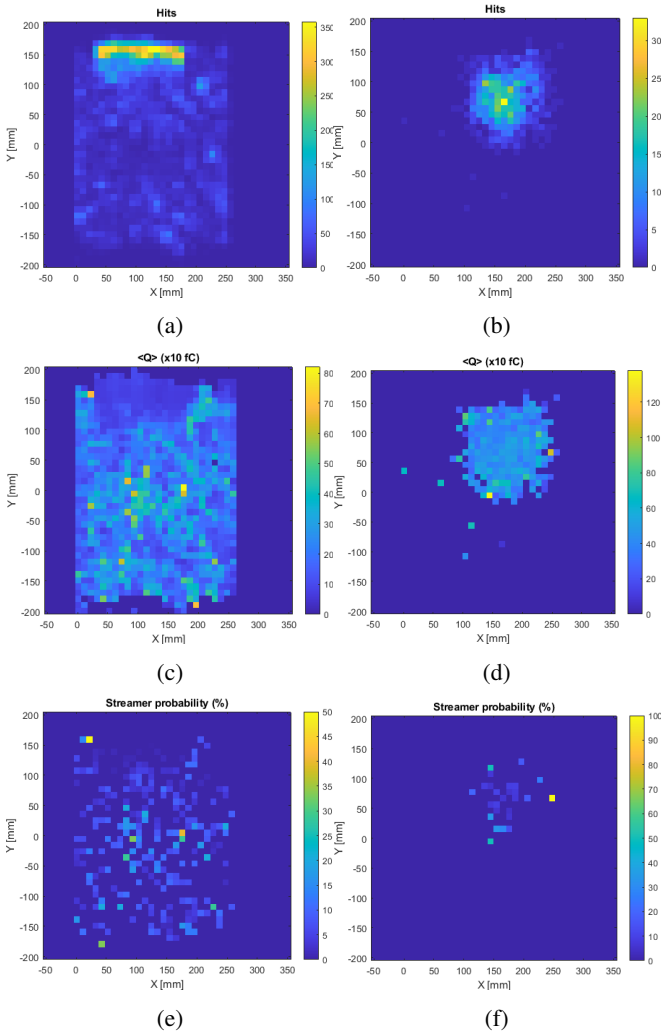

Figure 6: 2D plots: hits, average charge, and streamer probability for the RPC (right column) and Scintillator (left column) triggers as a function of the X and Y coordinates of the hits, for a HV of 6kV. In the plots (a), (c) and (e) correspond to the RPC trigger, while (b), (d) and (f) correspond to the Scintillator trigger.

plateau of the efficiency versus high voltage/gap, as demonstrated in Figure 3 of reference [5]. The detector efficiency was calculated as:

$$\varepsilon\,(\%) = \frac{\#\text{ events in RPC}}{\#\text{ in 4 Scintillators}} \tag{1}$$

Where the denominator corresponds to muon events selected by the four-fold scintillator coincidence, and the numerator includes only those also recorded by the sRPC.

To characterize the detector's spatial response, 2D maps were produced showing: the number of detected hits, the average collected charge and the streamer probability, all as functions of the reconstructed hit position (X, Y). Streamer probability was defined as the fraction of events exceeding 1.2 pC in total charge, a threshold used to differentiate streamers from avalanches.

Figure 6 shows these results. The right-hand column (Figures b, d, f) displays events triggered by the external scintillators, while the left-hand column (Figures a, c, e) corresponds to self-triggered events in the sRPC.

In the scintillator-triggered data, a well-defined cluster of hits is observed in the central-upper region of the detector (Figures b, d, f), matching the geometric projection of the telescope onto the sRPC. The collected charge is uniform, and the streamer probability is minimal, confirming a consistent and efficient response to minimum ionizing particles. In the self-triggered data, however, a markedly different pattern emerges.

The hit map (Figure a) shows a strong accumulation of events in the top-left region, which lies outside the telescope acceptance. While this may result from noise or localized effects near spacers, the highly concentrated and intense activity points to a possible detector defect, such as poor gap uniformity, non-uniform electrode coating, or partial breakdown in insulation. The average charge map (Figure c) appears broadly uniform, with no strong spatial modulation.

As introduced in Section 3.3, the sum of the two highest strip charges, instead of relying on the single-strip charge, improves the consistency of the charge measurement and provided a more accurate representation of the total induced sig-

nal. Importantly, this modification did not alter the detector efficiency, which remained around 98%, but it increased the measured streamer probability, as expected, since the combined charges more often exceeded the 1.2 pC threshold.

4 Results

The data were collected over approximately one year, enabling a long-term assessment of the sRPC performance under varying environmental conditions. Measurements were grouped into intervals of about 24 hours, during which the average charge, ambient temperature (°C), atmospheric pressure (mbar), and relative humidity (%) were determined.

The evolution as a function of time of the average charge (Figure. 7a) shows a clear inverse correlation with temperature (Figure. 7b). During the winter months, particularly in During the winter months, particularly in December 2024, the ambient temperature reached significantly low values. To prevent excessive cooling of the detector, a localized heater was installed near the sRPC on January 19, which corresponds to the abrupt trend observed in the January plots.

The atmospheric pressure (Figure. 8a) and relative humidity (Figure. 8b) also showed variations over the monitoring period.

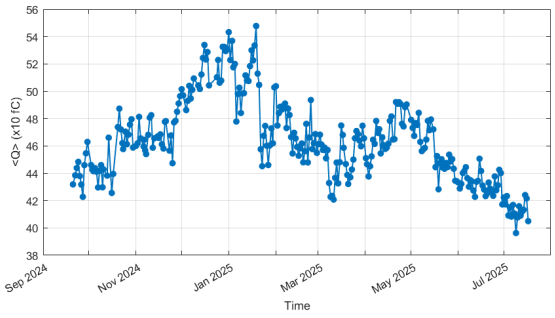

(a) Average charge in fC.

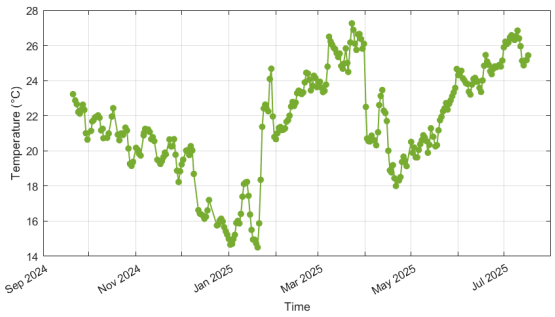

(b) Temperature in °C.

Figure 7: The evolution as a function of time of the average charge (a) and ambient temperature (b) between Sep-2024 and Jul-2025.

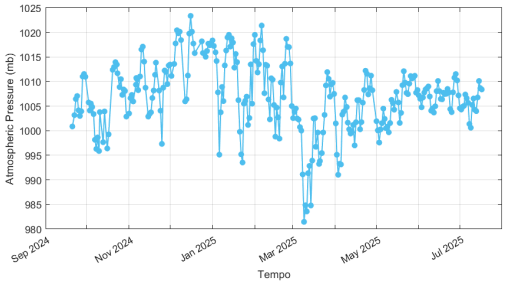

(a) Atmospheric Pressure in mbars.

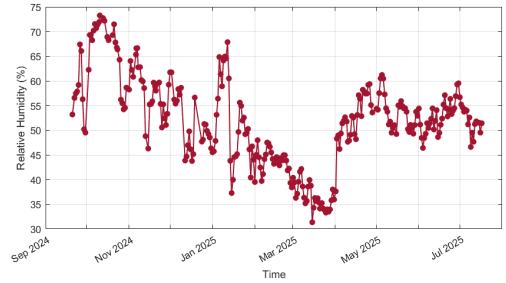

(b) Relative Humidity in %.

Figure 8: The evolution as a function of time of the atmospheric pressure (c) and relative humidity (d) between Sep-2024 and Jul-2025.

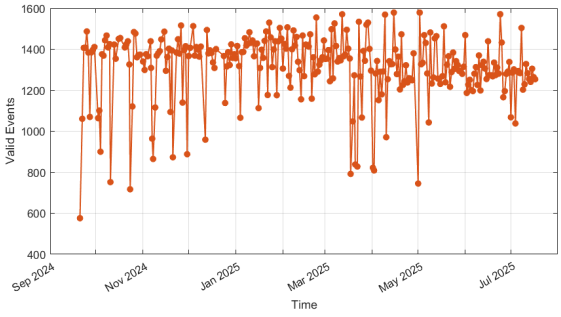

(a) Number of valid events.

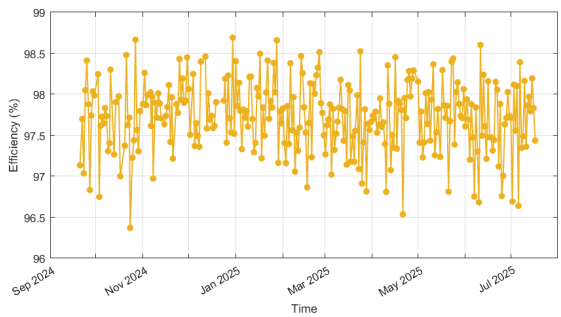

(b) Efficiency in %.

Figure 9: Operational behavior of the detector: (a) Number of valid events per day and (b) Detection efficiency.

Figure 9 summarizes the operational behavior of the detector throughout the acquisition period. Figure 9.a shows the number of valid events per day, which means, events that meet the muon-filtering criteria described in Section 3.4. The figure 9.b presents the corresponding detection efficiency, calculated as the ratio between the sRPC signals and the coincidence triggers from the scintillator telescope (Equation 1).

Figure 10.a displays the streamer probability, defined as the fraction of events with a total charge exceeding 1.2 pC. Finally, Figure 10.b shows the event rate, which appears to vary approximately in direct proportion to the temperature.

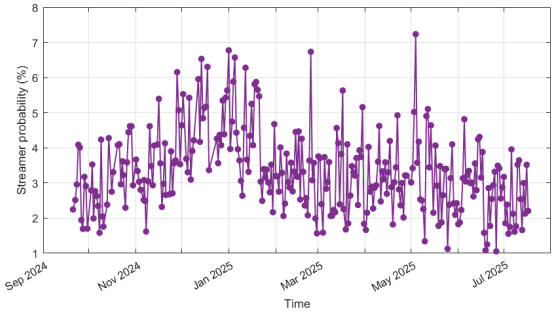

(a) Streamer probability in %.

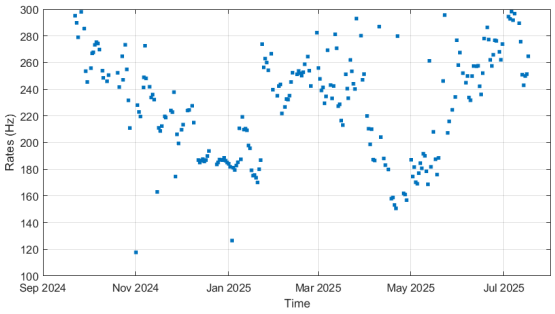

(b) Event rates.

Figure 10: Operational behavior of the detector: (a) Streamer probability and (b) Event rates, between Sep-2024 and Jul-2025.

This long-term monitoring aimed to study how variations of the environment affects the performance of a sealed RPC. To investigate these dependencies in greater detail, two-dimensional correlation plots were produced (Figures 11 and 12). Figure 11 illustrates the temperature as a function of average charge, with atmospheric pressure represented by a color scale; This plot clearly shows an inverse correlation, where the average charge decreases as temperature increases. Figure 12 presents the pressure as a function of average charge, with temperature values indicated for each point, revealing an approximately direct correlation between these two quantities.

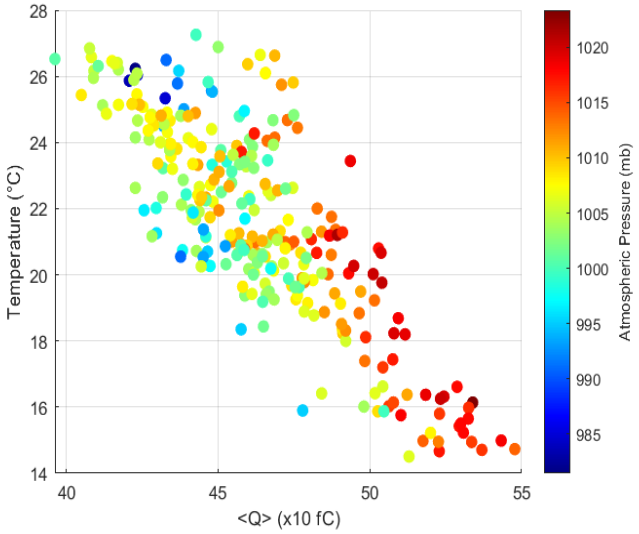

Figure 11: Correlation between average charge and temperature, showing the influence of atmospheric pressure (color scale).

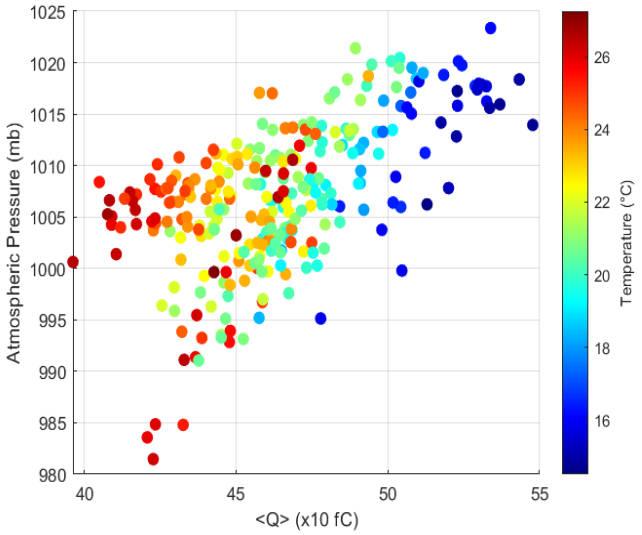

Figure 12: Correlation between average charge and pressure, showing the influence of temperature (color scale).

To decouple the effects of temperature and pressure, a linear correction procedure was applied. By performing independent fits of charge versus temperature and charge versus pressure (Figures 13 and 14), the respective slopes were subtracted, allowing the impact of each variable to be evaluated separately. Figure 15 shows the charge, expressed as a percentage, after removing the correlation with temperature, while Figure 16 displays the corresponding result after eliminating the influence of pressure.

A detailed analysis of these results confirms that the average induced charge $< Q >$ is inversely correlated with temperature and directly correlated with atmospheric pressure.

In a sealed RPC, an increase in ambient temperature leads to a reduction in gas density and an increase in internal pres-

sure, since the gas volume is fixed. This pressure rise induces mechanical stress on the detector structure, resulting in a slight expansion of the detector and an effective increase of the gas gap size, which in turn produces a decrease in the electric field and a reduction of the detector gain. Conversely, a decrease in temperature increases the gas density and reduces the internal pressure, leading to a contraction of the detector structure, a smaller effective gas gap, and a corresponding increase in the detector gain.

External pressure variations act as mechanical loads on the sealed detector. An increase in the external atmospheric pressure compresses the detector structure, reducing the effective gas gap size and increasing the electric field strength, which results in an enhancement of the detector gain. In contrast, a decrease in external pressure relieves the mechanical stress on the detector, allowing a slight expansion of the structure, an increase in the effective gas gap, and a consequent reduction in the detector gain.

These observations support the interpretation that, in sealed detectors, temperature- and pressure-induced mechanical deformations of the detector structure play a dominant role by modifying the effective gas gap, ultimately driving the observed gain variations.

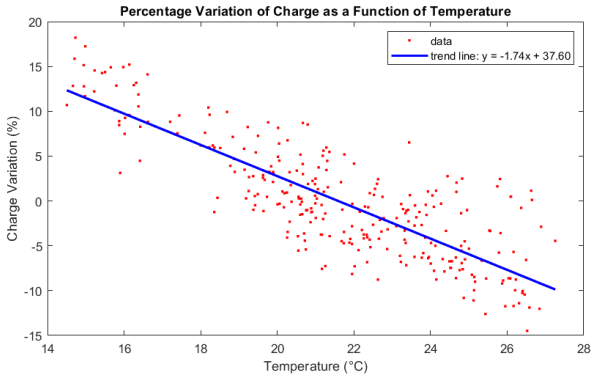

Figure 13: Linear fit of temperature as a function of average charge.

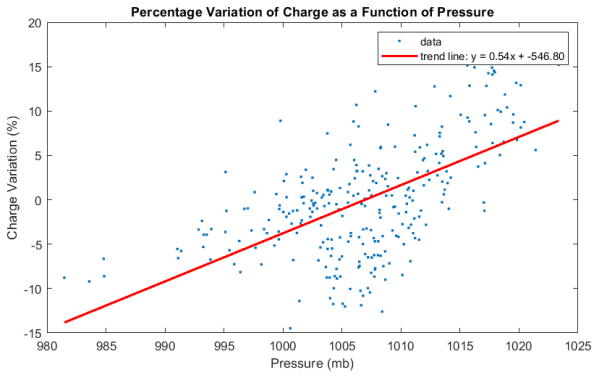

Figure 14: Linear fit of atmospheric pressure as a function of average charge.

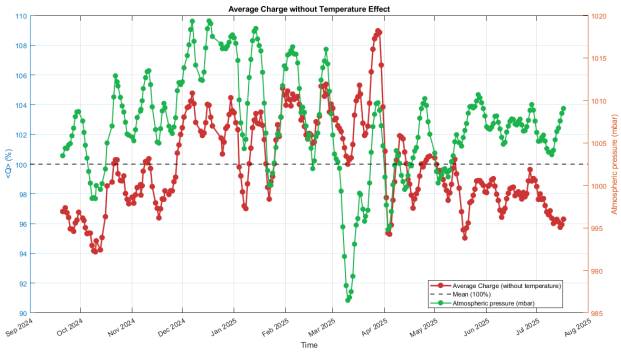

Figure 15: Average charge variation (in %) with temperature effects removed, showing pressure influence.

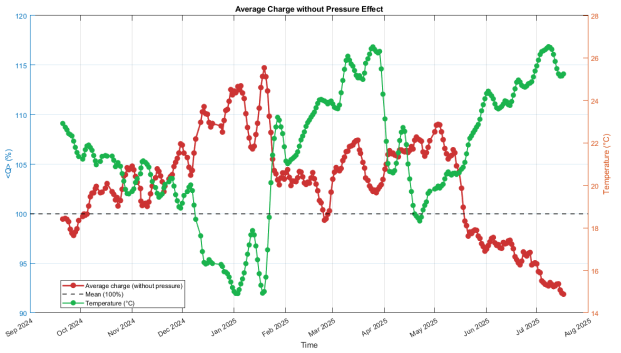

Figure 16: "Average charge variation (in %) with pressure effects removed, showing temperature influence.

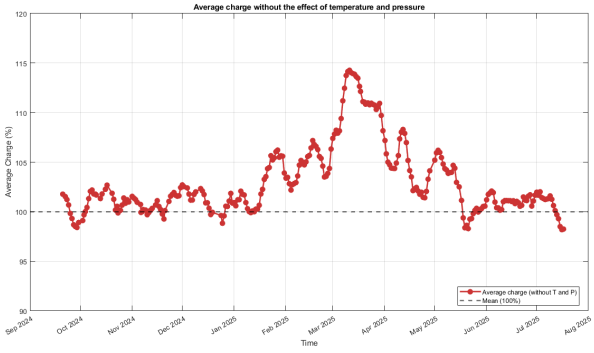

Figure 17: Percentage variation of average charge after environmental corrections.

Finally, Figure 17 shows the percentage variation of the induced charge after simultaneously correcting for both temperature and pressure effects. Ideally, these corrected values would fluctuate around a constant mean, indicating complete compensation for environmental influences. However, residual deviations persist, particularly at higher temperatures, suggesting the presence of additional effects impacting the detector response that are not yet fully understood. These findings highlight the need for further studies to fully characterize the environmental dependencies of sealed RPCs and to develop

more effective stabilization or correction methods for long-term operation.

5 Conclusions

This study investigated the environmental response of a sealed Resistive Plate Chamber (sRPC) prototype, revealing a clear inverse correlation between average induced charge and temperature, and a direct correlation with atmospheric pressure.A linear correction method was applied to compensate for these environmental effects, significantly reducing charge variations. However, residual deviations, particularly at elevated temperatures, suggest the presence of additional factors influencing detector performance. Further investigation and study are therefore required to fully characterize these effects.

Acknowledgements

We would like to express our heartfelt thanks to our supervisor, Alberto Blanco Castro, and the whole LIP team for an exceptionally rewarding summer internship. Their guidance and support made this journey both inspiring and impactful. This experience has been truly valuable and will have a lasting, positive influence on our future paths.

References

[1] A. Blanco, P. Fonte, L. Lopes, M. Pimenta, Nuclear Instruments and Methods in Physics Research Section A: Accelerators, Spectrometers, Detectors and Associated Equipment **1075**, 170 (2025)

[2] J. Pinto, M. Carvalho, T. Paes, LIP Internship Program 2024 (2024)

[3] C. Soneira-Landín, A. Blanco, L. Fraile, J.A. Garzón, G. Kornakov, L. Lopes, V. Nouvilas, J. Udías, Nuclear Instruments and Methods in Physics Research Section A: Accelerators, Spectrometers, Detectors and Associated Equipment **1077**, 170511 (2025)

[4] M. Böhmer, G. Korcyl, L. Maier, J. Michel, A. Neiser, M. Palka, M. Penschuck, P. Strzempek, M. Traxler, C. Ugur, *A Users Guide to the TRB3 and FPGA-TDC Based Platforms* (2025), version of July 18, 2025 - 12:00

[5] A. Blanco, M. Carvalho, S. Fetal, L. Lopes, T. Paes, J. Pinto, P. Fonte, Nuclear Instruments and Methods in Physics Research Section A: Accelerators, Spectrometers, Detectors and Associated Equipment p. 170743 (2025)